Cooperative coupling of cell-matrix and cell–cell adhesions in cardiac muscle

Megan L. McCain[a], Hyungsuk Lee[a,1], Yvonne Aratyn-Schaus[a], André G. Kléber[b], and Kevin Kit Parker[a,2]

[a]Disease Biophysics Group, Wyss Institute for Biologically Inspired Engineering, School of Engineering and Applied Sciences, Harvard University, Cambridge, MA 02138; and [b]Department of Pathology, Beth Israel Deaconess Medical Center, Harvard Medical School, Boston, MA 02215

Adhesion between cardiac myocytes is essential for the heart to function as an electromechanical syncytium. Although cell-matrix and cell–cell adhesions reorganize during development and disease, the hierarchical cooperation between these subcellular structures is poorly understood. We reasoned that, during cardiac development, focal adhesions mechanically stabilize cells and tissues during myofibrillogenesis and intercalated disc assembly. As the intercalated disc matures, we postulated that focal adhesions disassemble as systolic stresses are transmitted intercellularly. Finally, we hypothesized that pathological remodeling of cardiac microenvironments induces excessive mechanical loading of intercalated discs, leading to assembly of stabilizing focal adhesions adjacent to the junction. To test our model, we engineered µtissues composed of two ventricular myocytes on deformable substrates of tunable elasticity to measure the dynamic organization and functional remodeling of myofibrils, focal adhesions, and intercalated discs as cooperative ensembles. Maturing µtissues increased systolic force while simultaneously developing into an electromechanical syncytium by disassembling focal adhesions at the cell–cell interface and forming mature intercalated discs that transmitted the systolic load. We found that engineering the microenvironment to mimic fibrosis resulted in focal adhesion formation adjacent to the cell–cell interface, suggesting that the intercalated disc required mechanical reinforcement. In these pathological microenvironments, µtissues exhibited further evidence of maladaptive remodeling, including lower work efficiency, longer contraction cycle duration, and weakened relationships between cytoskeletal organization and force generation. These results suggest that the cooperative balance between cell-matrix and cell–cell adhesions in the heart is guided by an architectural and functional hierarchy established during development and disrupted during disease.

adherens junctions | sarcomere | mechanotransduction | extracellular matrix

In the adult heart, healthy ventricular tissue is characterized by spatial segregation of cell-matrix adhesions to transverse myocyte borders (1) and cell–cell adhesions to longitudinal myocyte borders (2). Many cardiomyopathies are characterized by lateralization of cell–cell adhesions (3–5), increased expression of cell-matrix adhesions (6, 7), and arrhythmogenesis (8), suggesting that spatially organized adhesion is essential for effective eletromechanical coupling (9). Although in vivo studies have shown that localization of cell-matrix and cell–cell adhesions is developmentally regulated (10–13), the factors that regulate their assembly and disassembly are not well understood.

Cell-matrix adhesions are especially important during organogenesis, anchoring developing cells and tissues to the extracellular matrix (ECM) (14) and directing cell migration (15–17). As development progresses, cell-matrix adhesions must selectively disassemble so that cell–cell adhesions can form (18). In the heart, this exchange of adhesion sites occurs while myocytes are contractile (19, 20), indicating that myofibrils, cell–cell, and cell-matrix adhesions must cooperatively remodel without compromising cardiac output. Because cell-matrix (21–24) and cell–cell adhesions (25, 26) are mechanosensitive, mechanical forces likely serve as cues for remodeling adhesions and assembling tissues. In vitro studies have demonstrated that cytoskeletal tension (27) and exogenous cyclic strain (28, 29) promote cell–cell adhesion and tissue assembly in many cell types. Culturing noncardiac cells on stiff substrates tips the balance of adhesion in favor of focal adhesions and away from cell–cell adhesions (30–32), suggesting that mechanical forces can modulate the assembly or disassembly of tissues. Many cardiomyopathies are characterized by increased fibrosis and tissue stiffening (33, 34), suggesting that cardiac myocytes might be similarly sensitive to tissue compliance and favor focal adhesion formation over cell–cell junction formation in a fibrotic microenvironment.

We hypothesized that focal adhesions mechanically stabilize myocytes during tissue assembly, when myofibrils are contractile but the intercalated disc is not yet fully assembled. We postulated that focal adhesions disassemble as intercalated discs mature such that systolic forces are transmitted intercellularly. Furthermore, we reasoned that stiff microenvironments potentiate excessive intrinsic loading that destabilizes the intercalated disc and induces focal adhesion formation near the cell–cell junction. We modeled developing, healthy, and diseased cardiac tissue by engineering µtissues composed of two neonatal rat ventricular myocytes on deformable substrates of tunable elasticity. To characterize progressive stages of tissue assembly, we cultured µtissues on physiological substrates and measured structural and functional outputs over time. µtissues gradually increased systolic force generation, disassembled focal adhesions near the cell–cell interface, and formed intercalated discs to transmit the systolic load. To mimic diseased myocardium, we cultured µtissues on stiff substrates and observed further increases in force generation, maladaptive functional remodeling, and focal adhesion formation adjacent to the cell–cell interface. These data suggest that regulation of cell-matrix and cell–cell adhesions during cardiac development is guided by an intrinsic hierarchy that is altered in disease due to mechanical remodeling of the microenvironment.

Results

ECM Regulates Cooperative Intra- and Intercellular Assembly. We hypothesized that focal adhesion attachments to the ECM are important in development for directing migration and myofibrillogenesis and stabilizing myocytes as they become contractile. However, we suspected that focal adhesions adjacent to the cell–cell junction disassemble once the intercalated disc is capable of transmitting systolic loads intercellularly. To test this model, we

BIOPHYSICS AND COMPUTATIONAL BIOLOGY

engineered rectangular µtissues consisting of two neonatal rat ventricular myocytes on micropatterned fibronectin (FN) islands and monitored them over time. Eight hours after seeding, spreading myocytes typically protruded along a lateral edge of the island, independent of whether one (Fig. 1*A*) or two myocytes (Fig. 1*B*) adhered to the island. After 12 h, µtissues filled the island and striated myofibrils and sigmoid-like cell–cell interfaces were observable (Fig. 1 *C* and *D*). In contrast, myocytes on substrates coated with uniform FN extended randomly oriented protrusions before forming confluent, isotropic monolayers (Fig. S1 *A–C*). Cell–cell junctions were relatively linear (Fig. S1*D*) and perpendicular to myofibrils, characteristic of junctions in vivo (2). These results indicate that cell-ECM interactions guide cell spreading and myofibrillogenesis early in tissue assembly, influencing cell–cell junction formation by regulating myocyte shape.
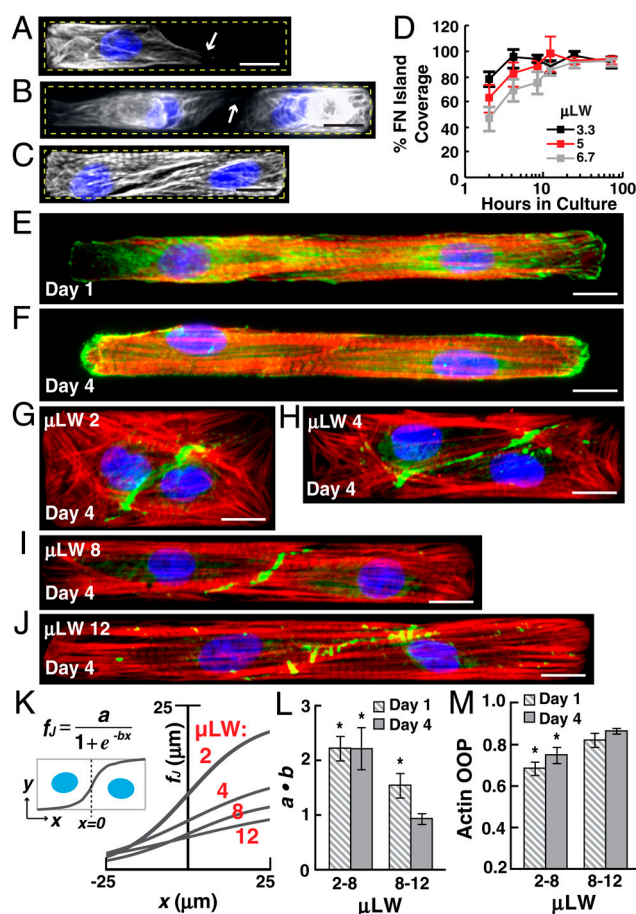

Fig. 1. µTissue formation on micropatterned FN islands. Single (*A*) and paired (*B*) myocytes cultured for 8 h on FN islands typically protruded (white arrows) along edges of the FN pattern (yellow dashed lines). (*C*) Twelve hours after seeding, µtissues covered FN islands and striated myofibrils were apparent (white: actin, blue: nuclei). (Scale bars: 10 µm.) (*D*) Time-dependent measurements of island coverage for µtissues with length to width ratios (µLW) of 3.3, 5, and 6.7 indicate that myocyte spreading was complete after 12 h. Bars = standard error; n ≥ 4 at each point. Representative Day 1 (*E*) and 4 (*F*) µtissues stained for actin (red), paxillin (green), and nuclei (blue). (Scale bars: 10 µm.) β-Catenin immunostains (green: β-catenin, red: actin, blue: nuclei) for representative Day 4 µtissues cultured on polydimethylsiloxane coverslips with µLW 2 (*G*), 4 (*H*), 8 (*I*), and 12 (*J*) demonstrate that cell–cell junctions had sigmoid-like contours. (Scale bars: 10 µm.) (*K*) Cell–cell junction contours were fit to the logistic function for a sigmoid curve, defined as f_J. The average f_J for each µLW is plotted. Average (*L*) $a \cdot b$ of f_J and (*M*) actin OOP, which ranges from 0 for isotropic to 1 for perfectly aligned systems, are plotted for Day 1 and 4 µtissues grouped by µLW 2–8 and 8–12. Bars = standard error; *p < 0.05 relative to µLW 8–12, Day 4 group; n ≥ 8 for each group.

Although focal adhesions are critical early in tissue assembly, we reasoned that focal adhesions near the cell–cell interface disassemble as adjacent intercalated discs establish intercellular mechanical continuity. To investigate this, we immunostained for paxillin to monitor differences in focal adhesion localization between µtissues cultured on micropatterned polyacrylamide gels with physiological stiffness (13 kPa) (35) for 1 d (Day 1) and 4 d (Day 4) to represent immature and mature tissues, respectively. At Day 1 (Fig. 1*E*), paxillin signal, although relatively diffuse, was detected in plaques at the longitudinal ends of the µtissue, colocalized with terminating myofibrils. Paxillin plaques were also detected near the cell–cell interface, suggestive of focal adhesion formation. At Day 4 (Fig. 1*F*), paxillin signal was localized to the longitudinal ends of the µtissue in larger and more distinct plaques. Near the cell–cell interface, paxillin signal appeared relatively weak, suggesting that focal adhesions near the cell–cell interface disassembled over the course of tissue maturation.

Because both cell-matrix and cell–cell adhesions anchor the cytoskeleton, we reasoned that cell–cell junction morphology is constrained by cell-matrix adhesions and regulated by the stage of tissue assembly. In Day 1 and 4 µtissues, the cell–cell junction had a sigmoid-like contour, similar to yin-yang interfaces observed in migrating endothelial cells constrained to FN islands (17) and diagonal interfaces in patterned myocyte pairs (36). To quantify this, we measured junction geometry while varying µtissue length to width ratio (µLW) (Fig. 1 *G–J*). We defined the longitudinal and transverse axis of the µtissue as the *x* and *y* axis, respectively, and fit the junction to the logistic function for a sigmoid curve, $f_J = \frac{a}{1+e^{-bx}}$. The quantity $a \cdot b$ represents slope at the µtissue center, where $x = 0$ (Fig. 1*K*). We grouped together µLW 2–8 and 8–12 and found that, at both Day 1 and 4, slope was lower for µLW 8–12 compared to µLW 2–8 (Fig. 1*L*). Junction slope decreased between Day 1 and 4 for µLW 8–12 (Fig. 1*L*), likely because myocytes were still remodeling their adhesions and myofibrils at this early time point. We quantified time-dependent changes in cytoskeletal architecture by calculating the actin orientational order parameter (OOP), which ranges from 0 for isotropic to 1 for perfectly aligned systems (37), and found a slight, but not statistical, increase in actin OOP between Day 1 and 4 for µLW 2–8 and 8–12 (Fig. 1*M*). At both Day 1 and 4, the OOP for µLW 8–12 was higher than µLW 2–8 due to increased myofibril alignment at higher µLW. These data suggest that myofibrillogenesis and remodeling of cell-matrix and cell–cell adhesions are cooperative processes in cardiac development.

Systolic Force Output Increases as Tissues Assemble. Based on our structural data, we reasoned that the magnitude of peak systolic traction force transmitted to the ECM near the cell–cell interface decreased as µtissues disassembled focal adhesions, formed mature cell–cell junctions, and transmitted systolic forces intercellularly. To generate traction stress vector maps of the substrate, we cultured µtissues on micropatterned polyacrylamide gels (13 kPa) doped with fluorescent microbeads for traction force microscopy (TFM) (38). With each spontaneous contraction, µtissues deformed the gel and displaced the fluorescent beads, which was captured with a CCD camera at 40 Hz. Bead displacement was measured, yielding displacement vector maps used to calculate traction stress vector maps during contraction and relaxation (37, 38). Following TFM measurements, µtissues were immunostained for actin, β-catenin, and nuclei to examine cytoskeletal structure and identify the cell–cell junction. At Day 1 (Fig. 2 *A* and *B*), we detected peak systolic traction stresses at the longitudinal ends of the µtissue and near the cell–cell interface, consistent with the presence of focal adhesions. At Day 4 (Fig. 2 *C* and *D*), peak systolic traction stresses were reduced, or not detected, near the cell–cell interface, suggesting that contractile force was transmitted primarily through the cell–cell
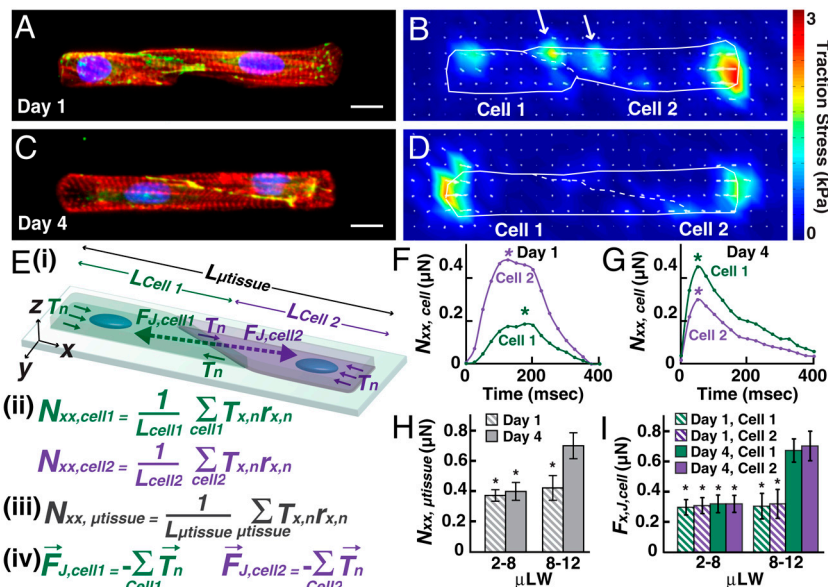
Fig. 2. Remodeling of force generation and transmission in developing cardiac μtissues. (A) Day 1 μtissue stained for actin (red), β-catenin (green), and nuclei (blue). The corresponding peak systolic traction stress vector map (B) revealed that cell 2 generated substantial traction against the substrate near the cell–cell interface (white arrows). Conversely, a Day 4 μtissue (C, same staining protocol as A) showed negligible traction stress near the cell–cell interface at peak systole (D). (B and D) Solid white line: μtissue outline; dashed white line: junction outline. (Scale bars: 10 μm.) (E, i) Schematic (not drawn to scale) and (ii) equations used to calculate $N_{xx,\text{cell1}}$ and $N_{xx,\text{cell2}}$, (iii) $N_{xx,\mu\text{tissue}}$, and (iv) $\vec{F}_{J,\text{cell1}}$ and $\vec{F}_{J,\text{cell2}}$. Plots of $N_{xx,\text{cell1}}$ and $N_{xx,\text{cell2}}$ for the (F) Day 1 and (G) Day 4 μtissues shown in A and B and C and D, respectively, during a single contraction cycle. Asterisks indicate peak systole for each myocyte, which occur at different time points in F, but not G. Average (H) $N_{xx,\mu\text{tissue}}$ and (I) $F_{x,J,\text{cell1}}$ and $F_{x,J,\text{cell2}}$ as a function of day in culture and μLW. Bars = standard error; *p < 0.05 relative to μLW 8–12, Day 4 group; $n \geq 6$ μtissues per group.

junction instead of focal adhesions. Based on the location of the β-catenin immunosignal, we determined traction stress vectors contributed by each myocyte, calculated traction force vectors ($\vec{T}_n$) by multiplying traction stress at each grid point n by the grid unit surface area, and calculated the average longitudinal tension through a cross-section of each myocyte ($N_{xx,\text{cell}}$) (Fig. 2E). We plotted $N_{xx,\text{cell1}}$ and $N_{xx,\text{cell2}}$ through a single contraction cycle for the Day 1 (Fig. 2F) and 4 (Fig. 2G) μtissues shown in Fig. 2A and B and Fig. 2C and D, respectively. In the Day 1 μtissue, myocytes were slightly out of phase and reached peak systole at different time points, suggestive of weak electrical coupling (Movie S1). Conversely, in the Day 4 μtissue, myocytes reached peak systole simultaneously (Movie S2), implying electrical continuity across the cell–cell junction. To confirm electrical coupling on Day 4, we measured intercellular electrical conductance between myocytes with dual voltage clamp (Fig. S2 A–C) and detected Cx43 immunosignal in punctate clusters along the cell–cell interface (Fig. S2 D and E), demonstrating that μtissues had electrical continuity via gap junction channels (39). These results suggest that, between Day 1 and 4, myocytes become synchronous and transmit force across the cell–cell junction instead of to the ECM near the cell–cell interface, indicative of focal adhesion disassembly and intercalated disc maturation.

To correlate adhesion remodeling to systolic force generation, we calculated the average longitudinal tension through a cross-section in Day 1 and 4 μtissues ($N_{xx,\mu\text{tissue}}$) and adapted a previously published method (40) to calculate forces exerted against the junction by cells 1 ($\vec{F}_{J,\text{cell1}}$) and 2 ($\vec{F}_{J,\text{cell2}}$) (Fig. 2E). Because each myocyte must be in mechanical equilibrium, the vectorial sum of $\vec{T}_n$ associated with each myocyte indicates the force exerted against the cell–cell junction ($\vec{F}_{J,\text{Cell}} = -\sum_{\text{Cell}} \vec{T}_n$) (Fig. 2E). The magnitude of the x-component of $\vec{F}_{J,\text{Cell}}$ indicates the longitudinal cell–cell junction force ($F_{x,J,\text{Cell}} = |\sum_{\text{Cell}} T_{x,n}|$). As shown in Fig. 2 H and I, $N_{xx,\mu\text{tissue}}$, $F_{x,J,\text{cell1}}$, and $F_{x,J,\text{cell2}}$ did not change between Day 1 and 4 for μLW 2–8. However, $N_{xx,\mu\text{tissue}}$, $F_{x,J,\text{cell1}}$, and $F_{x,J,\text{cell2}}$ increased significantly between Day 1 and 4 for μLW 8–12, likely because myofibrils are longer

at higher μLW and require more time to mature. Thus, in μtissues with high μLW, systolic force generation increases while adjacent focal adhesions disassemble and intercalated discs mature, indicating that force generation and tissue formation occur on similar time scales and are potentially linked.

Stiff Microenvironments Induce Maladaptive Remodeling of Contractile Function. Cardiac myocytes remodel in response to changes in the physical microenvironment. For example, the elastic modulus of embryonic cardiac tissue ranges from 1–6 kPa and increases to 10–15 kPa in the adult heart, which is reported to increase beating rate, myofibril maturation, and work output in cultured myocytes (35, 41). Increases in tissue stiffness beyond 50 kPa are characteristic of many cardiomyopathies due to excessive fibrosis (33), which is reported to inhibit contraction and promote stress fiber formation in vitro (35, 41) and exceeds the elastic modulus of isolated, relaxed myofibrils (42). We hypothesized that increased stiffness of the cardiac microenvironment induces maladaptive remodeling of contractile function and alters the balance between cell-matrix and cell–cell adhesion. To test this, we performed TFM and paxillin immunostaining on μtissues cultured on gels with low (1 kPa), moderate (13 kPa), and stiff (90 kPa) elastic moduli to characterize stiffness-dependent changes to contractile function and focal adhesion formation. With increasing elastic modulus, peak systolic displacement decreased, force generation increased, and focal adhesion size at the longitudinal ends increased (Fig. 3 A–C). Stiffness-dependent changes to displacement and stress generation are illustrated by the slopes of traces relating the maximum traction stress vector (max.$|\sigma_{x,\mu\text{tissue}}|$) to the maximum displacement vector (max.$|\Delta x_{\mu\text{tissue}}|$) in the longitudinal direction (Fig. 4A). By plotting peak systolic $N_{xx,\mu\text{tissue}}$, $F_{x,J,\text{cell1}}$, and $F_{x,J,\text{cell2}}$ for each stiffness (Fig. 4B), we found a relationship analogous to the Frank–Starling law, where force generation increases in response to increased load (43) or mechanical stretch (44). We also calculated average peak systolic work as a function of stiffness, which is an important parameter for evaluating cardiac function because effective pumping is
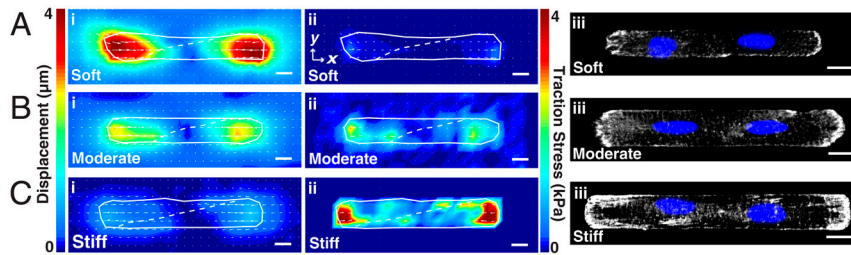
Fig. 3. Regulation of displacement, traction stress, and focal adhesion formation by substrate stiffness. Displacement vector maps (*i*), traction stress vector maps (*ii*), and paxillin immunostains (*iii*) for representative μtissues with μLW 8 on (*A*) soft (1 kPa), (*B*) moderate (13 kPa), and (*C*) stiff (90 kPa) substrates (*C*). For *A–C*, *i* and *ii* are from the same μtissue and *iii* is from a different μtissue. Blue: nuclei. (Scale bars: 10 μm.).

dependent on force generation and shortening. We found that peak systolic work increased from soft to moderate substrates but did not further increase from moderate to stiff substrates (Fig. 4*B*). Thus, μtissues on stiff substrates generate significantly more force to produce similar magnitudes of work as on moderate substrates.

Previous reports observed that contraction cycle duration is prolonged in aging myocardium (45, 46) and that force-frequency relationships are defective in heart failure models (47). We asked if microenvironmental elasticity regulates contraction cycle dynamics. The duration of contraction, averaged for all μLW on each stiffness, increased as the substrate stiffened, although only soft and stiff substrates were statistically different (Fig. 4*C*). Furthermore, μtissues on stiff substrates had prolonged peak systole (Fig. S3), similar to previous reports (35).

In addition to changes in tissue compliance, cardiac disease is associated with remodeling of myocyte shape and cytoskeletal

architecture (48), which is thought to be a compensatory response to mechanical overload (49). We asked if substrate stiffness affects relationships between tissue geometry and force generation to determine if the physical microenvironment affects intrinsic compensatory mechanisms. We grouped together μLW 2–4, 4–8, and 8–12 and found that, on soft and moderate substrates, peak systolic $N_{xx,\mu\text{tissue}}$ was highest at μLW 8–12 (Fig. 4*D*), likely because myofibril length and alignment are maximized. The sample size for μLW 8–12 on soft substrates is low ($n = 2$) because these μtissues typically generated enough force to deform the highly compliant substrate out of the microscope focal plane, hindering two-dimensional TFM. Our data are likely the weakest of the population, explaining the lack of significance between μLW 4–8 and 8–12. Interestingly, peak systolic $N_{xx,\mu\text{tissue}}$ was not dependent on μLW for stiff substrates (Fig. 4*D*), suggesting that substrate stiffness dominates over tissue architecture when the elastic modulus is very high. We also quantified actin OOP and cell–cell junction slope for μtissues on each substrate to identify any structural variability that could contribute to these functional differences and found that both parameters were independent of stiffness (Fig. S4). Collectively, these data show that, although stiff microenvironments increase force generation, the overall effect is maladaptive, as demonstrated by decreased work efficiency, increased contraction cycle duration, and weakened relationship between cytoskeletal organization and force generation.
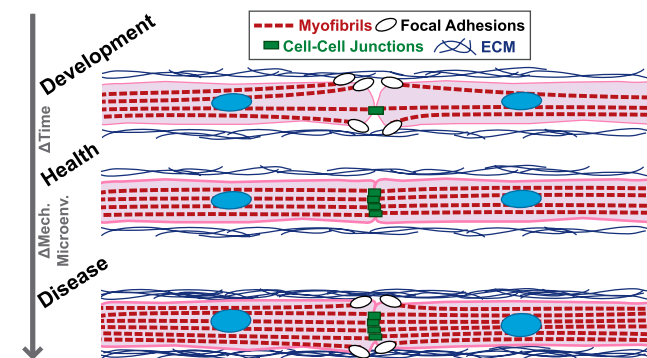
Focal Adhesions Reinforce Cell–Cell Junctions in Stiff Microenvironments. Diseased cardiac tissue is characterized by remodeling of cell-ECM and cell–cell adhesions (3–7) and decreased tissue compliance (33). We asked if stiff microenvironments affect the balance between cell–cell and cell-matrix adhesions, as reported for noncardiac cells (30–32). On stiff substrates, we often observed traction force and focal adhesions near the cell–cell interface (Fig. 3*C*), similar to Day 1 μtissues (Fig. 2*B*), suggesting that μtissues on stiff substrates have increased focal adhesion formation near the cell–cell interface. To quantify differences in force transmission to the cell–cell junction relative to the ECM for a given μtissue, we calculated the ratio of $F_{x,J,\text{cell}}$ to $N_{xx,\text{cell}}$ at peak systole for each myocyte and averaged together $\frac{F_{x,J,\text{Cell}}}{N_{xx,\text{Cell}}}$ from both myocytes ($\frac{F_{x,J,\text{cell}}}{N_{xx,\text{cell}}} = (\frac{F_{x,J,\text{Cell1}}}{N_{xx,\text{Cell1}}} + \frac{F_{x,J,\text{Cell2}}}{N_{xx,\text{Cell2}}})/2$). On moderate substrates, peak systolic $\frac{F_{x,J,\text{cell}}}{N_{xx,\text{cell}}}$ significantly increased between μLW 2–8 and 8–12 (Fig. 4*E*), indicating that μtissues with high μLW transmit relatively more force to the cell–cell junction than the ECM. For all μLW, peak systolic $\frac{F_{x,J,\text{cell}}}{N_{xx,\text{cell}}}$ was not statistically different between soft and moderate substrates. However, peak systolic $\frac{F_{x,J,\text{cell}}}{N_{xx,\text{cell}}}$ was significantly lower on stiff compared to moderate substrates at μLW 8–12, indicating decreased force transmission to the cell–cell junction relative to the ECM. On stiff substrates, peak systolic $\frac{F_{x,J,\text{cell}}}{N_{xx,\text{cell}}}$ was similar between μLW 2–8 and 8–12, indicating that this parameter is not regulated by μLW on stiff substrates. Our results suggest that, in stiff microenvironments, cardiac myocytes generate more force, which excessively loads the intercalated disc. This triggers focal adhesion assembly
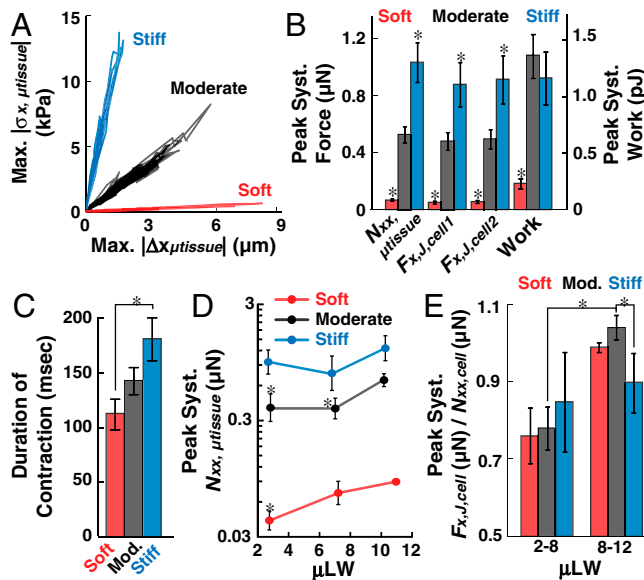
Fig. 4. Substrate stiffness regulates contractile function and balance of cell–cell and cell-matrix adhesion. (*A*) Magnitudes of maximum stress vectors in the *x*-direction (max.$|\sigma_{x,\mu\text{tissue}}|$) plotted against magnitudes of maximum displacement vectors in the *x*-direction (max.$|\Delta x_{\mu\text{tissue}}|$) for multiple μtissues during contraction cycles. (*B*) Average peak systolic $N_{xx,\mu\text{tissue}}$, $F_{x,J,\text{cell1}}$, $F_{x,J,\text{cell2}}$, and work plotted for μtissues on each stiffness. Bars = standard error; *$p < 0.05$ relative to moderate substrates; $n \geq 11$ μtissues for each stiffness. (*C*) Average duration of contraction for μtissues on each stiffness. Bars = standard error; *$p < 0.05$; $n \geq 10$ for each stiffness. (*D*) Peak systolic $N_{xx,\mu\text{tissue}}$ plotted as a function of μLW for μtissues grouped by μLW 2–4 (soft: n = 4, moderate: n = 5, stiff: n = 4), 4–8 (soft: n = 4, moderate: n = 6, stiff: n = 3), and 8–12 (soft: n = 2, moderate: n = 9, stiff: n = 5). Bars = standard error; *$p < 0.05$ relative to μLW 8–12 for the same stiffness. (*E*) Average peak systolic $F_{x,J,\text{cell}}/N_{xx,\text{cell}}$ for μtissues grouped by μLW 2–8 (soft: n = 8, moderate: n = 11, stiff: n = 7) and 8–12 (soft: n = 2, moderate: n = 9, stiff: n = 6). Bars = standard error; *$p < 0.05$.

McCain et al.

Fig. 5. Hypothesized schematic of cooperative coupling of cell-matrix and cell–cell adhesions in cardiac muscle. During development, focal adhesions guide migration and cell–cell junctions are assembling. In health, cell–cell junctions dominate over focal adhesions near the cell–cell interface and forces are transmitted intercellularly. In disease, when the microenvironment is stiff, focal adhesions reassemble near the cell–cell interface to stabilize excessively loaded cell–cell junctions.

adjacent to the cell–cell interface as a maladaptive means of structurally reinforcing the cell–cell junction, with the potential to disrupt mechanotransduction within the tissue.

Discussion

Remodeling of cell-matrix and cell–cell adhesions is important during cardiac development and disease. Here, we engineered cardiac µtissues in vitro to characterize the dynamic organization and functional remodeling of myofibrils, cell–cell, and cell-matrix adhesions during morphogenesis and pathogenesis. Our hypothesis for developmental and pathological regulation of adhesions is illustrated in Fig. 5. At early stages of tissue formation, we observed focal adhesion disassembly near the cell–cell interface coincident with maturation of the intercalated disc and transmission of systolic forces across the cell–cell boundary, suggesting that mature, healthy cardiac tissues preferentially form and maintain cell–cell junctions instead of focal adhesions at their longitudinal borders. On stiff substrates, we observed focal adhesion formation adjacent to the cell–cell interface, suggesting that fibrotic microenvironments destabilize cell–cell adhesion due to increased force generation, which stimulates focal adhesion formation.

In the heart, cell-matrix adhesions anchor maturing cells and tissues to the ECM (14) and direct cell migration and morphogenesis (15–17); however, robust cell–cell adhesion is critical to the primary function of many tissues, including barrier function of blood vessel endothelium (50) and formation of an electromechanical syncytium in the heart (9). Our model system recapitulates in vivo observations that focal adhesions decrease as cell–cell junctions increase at longitudinal myocyte borders during cardiac development (10–13). Our data combined with previous reports suggests that cell-matrix adhesions are critical early in development before cell–cell adhesions are fully mature; however, as development progresses, cell–cell adhesions are ultimately favored at longitudinal myocyte borders, suggestive of a developmentally regulated hierarchy of adhesion that drives the assembly and maintenance of well-coupled tissues.

In noncardiac preparations, increases in substrate stiffness promote cell–cell decoupling and focal adhesion formation (30–32). Similarly, many cardiomyopathies, such as myocardial infarction, are characterized by increased fibrosis and tissue stiffening (33, 34), increased integrin expression (6, 7), and uncoupling between myocytes (3–5), indicating that myocytes increase matrix adhesion while decreasing cell–cell adhesion. Our results suggest that stiffness-mediated increases in force generation necessitate compensatory assembly of focal adhesions adjacent to the intercalated disc to structurally reinforce the junction, which

is consistent with reports that cadherin–cadherin adhesions have lower failure strengths than integrin-ECM adhesions (51–53).

On stiff substrates, several functional parameters of µtissues deviated from those on physiological substrates, providing new insight into stiffness-dependent maladaptive remodeling. First, because µtissues on stiff substrates generated more force to attain similar magnitudes of work as on moderate substrates, energy demands in stiff microenvironments are likely greater, which could contribute to metabolic remodeling that accompanies cardiomyopathies such as pathological hypertrophy (54). Second, contraction cycle duration increased on stiff substrates, similar to observations in aging myocardium (45, 46), suggesting that decreased tissue compliance is sufficient to disrupt contraction cycle dynamics and could contribute to altered force-frequency relationships (47). Finally, the average peak systolic longitudinal tension generated by µtissues was uncorrelated to tissue geometry only on stiff substrates, suggesting that structural remodeling of myocyte shape, which is an important compensatory mechanism, is adaptive only in cellular microenvironments with mechanical compliances corresponding to the healthy heart.

In similar studies, the cell–cell junction force exerted by nonmyocytes ranged from 20 to 200 nN (27, 40). We measured peak systolic junction forces up to 1,000 nN in cardiac µtissues on physiological substrates, suggesting that cardiac intercalated discs are exposed to substantially higher forces than cell–cell junctions in other organs, potentially explaining why the heart is especially vulnerable to mutations of cell–cell adhesion proteins, such as desmoplakin (55–57). Beyond playing a role in tissue assembly, mechanical forces activate mechanotransduction and signaling at adhesion sites (22–26), indicating that cellular physiology could be affected by altered force transmission. Furthermore, because cell–cell junctions are critical for gap junction formation (58), stiffness-dependent remodeling of cell–cell adhesion could contribute to gap junction redistribution and arrhythmogenesis associated with many cardiomyopathies (3–5, 8). In summary, these results suggest that cell-matrix adhesions are important for directing myofibrillogenesis during early development but are progressively replaced with cell–cell adhesions at longitudinal myocyte borders as the tissue matures and preferentially transmits systolic loads intercellularly. This functional hierarchy can be perturbed in disease due to increased stiffness of the microenvironment, with focal adhesion assembly near the cell–cell interface indicative of a compensatory effort by the myocyte to maintain the structural integrity of the tissue.

Materials and Methods

Experimental methods are described in detail in the *SI Materials and Methods*; a brief description is included here.

Micropatterning of Polyacrylamide Gels. Fibronectin was cross-linked with biotin using Sulfo-NHS-LC-Biotin (Pierce). Polyacrylamide gel substrates were fabricated with the following elastic moduli and acrylamide/bis concentrations: 1 kPa: 5/0.1%; 13 kPa: 7.5/0.3%; 90 kPa: 12/0.6% (59). Elastic moduli were verified with atomic force microscopy (60) (Fig. S5 *A and B*). Streptavidin-acrylamide and 200 nm fluorescent beads were added to the gel solution for a final concentration of 1:5 and 1:100, respectively, by volume. Polyacrylamide gels were cured on activated 25 mm coverslips and microcontact printed (61) with biotinylated FN (62) after carefully drying the gel surface by incubating at 37 °C for 10 min (Fig. S5C).

Cell Culture. All procedures were conducted according to the guidelines of the Harvard University Animal Care and Use Committee. Ventricular myocytes from 2-d-old Sprague–Dawley rat hearts were isolated and cultured using previously described protocols (37, 39). 15,000–50,000 cells/cm² were seeded on substrates. Epinephrine (0.2 µM) was added for the first and last 24 h in culture to maintain spontaneous beating.

Traction Force Microscopy. High-resolution TFM was used to image bead displacement in spontaneously contracting myocytes cultured on micropatterned polyacrylamide gel substrates (37, 38). Following the experiment,

coverslips were fixed, immunostained for β-catenin, and imaged to identify the cell–cell junction. Methods used to acquire displacement and traction stress vectors from bead displacement images have been previously described (37, 38). The traction stress field was calculated from the displacement map using Fourier transform traction cytometry methods. The techniques used to calculate $N_{xx,\text{cell}}$, $\bar{F}_{J,\text{cell}}$, and $N_{xx,\mu\text{tissue}}$ are described in detail in the *SI Materials and Methods*.

Statistics. Data are displayed as mean ± standard error. Data were statistically analyzed using student's *t*-test, with $p < 0.05$ considered significant.

1. Anastasi G, et al. (2009) Dystrophin-glycoprotein complex and vinculin-talin-integrin system in human adult cardiac muscle. *Int J Mol Med* 23:149–159.
2. Gourdie RG, Green CR, Severs NJ (1991) Gap junction distribution in adult mammalian myocardium revealed by an anti-peptide antibody and laser scanning confocal microscopy. *J Cell Sci* 99:41–55.
3. Matsushita T, et al. (1999) Remodeling of cell–cell and cell–extracellular matrix interactions at the border zone of rat myocardial infarcts. *Circ Res* 85:1046–1055.
4. Kostin S, et al. (2003) Gap junction remodeling and altered connexin43 expression in the failing human heart. *Mol Cell Biochem* 242:135–144.
5. Smith JH, Green CR, Peters NS, Rothery S, Severs NJ (1991) Altered patterns of gap junction distribution in ischemic heart disease. An immunohistochemical study of human myocardium using laser scanning confocal microscopy. *Am J Pathol* 139:801–821.
6. Terracio L, et al. (1991) Expression of collagen binding integrins during cardiac development and hypertrophy. *Circ Res* 68:734–744.
7. Heling A, et al. (2000) Increased expression of cytoskeletal, linkage, and extracellular proteins in failing human myocardium. *Circ Res* 86:846–853.
8. Li J, Patel VV, Radice GL (2006) Dysregulation of cell adhesion proteins and cardiac arrhythmogenesis. *Clin Med Res* 4:42–52.
9. Kleber AG, Rudy Y (2004) Basic mechanisms of cardiac impulse propagation and associated arrhythmias. *Physiol Rev* 84:431–488.
10. Angst BD, et al. (1997) Dissociated spatial patterning of gap junctions and cell adhesion junctions during postnatal differentiation of ventricular myocardium. *Circ Res* 80:88–94.
11. Peters NS, et al. (1994) Spatiotemporal relation between gap junctions and fascia adherens junctions during postnatal development of human ventricular myocardium. *Circulation* 90:713–725.
12. Hirschy A, Schatzmann F, Ehler E, Perriard JC (2006) Establishment of cardiac cytoarchitecture in the developing mouse heart. *Dev Biol* 289:430–441.
13. Wu JC, Sung HC, Chung TH, DePhilip RM (2002) Role of N-cadherin- and integrin-based costameres in the development of rat cardiomyocytes. *J Cell Biochem* 84:717–724.
14. Baker EL, Zaman MH (2010) The biomechanical integrin. *J Biomech* 43:38–44.
15. Parker KK, et al. (2002) Directional control of lamellipodia extension by constraining cell shape and orienting cell tractional forces. *FASEB J* 16:1195–1204.
16. Ridley AJ, et al. (2003) Cell migration: Integrating signals from front to back. *Science* 302:1704–1709.
17. Huang S, Brangwynne CP, Parker KK, Ingber DE (2005) Symmetry-breaking in mammalian cell cohort migration during tissue pattern formation: Role of random-walk persistence. *Cell Motil Cytoskeleton* 61:201–213.
18. Harris TJ, Tepass U (2010) Adherens junctions: From molecules to morphogenesis. *Nat Rev Mol Cell Biol* 11:502–514.
19. Woods JR, Jr, Dandavino A, Brinkman CR, 3rd, Nuwayhid B, Assali NS (1978) Cardiac output changes during neonatal growth. *Am J Physiol* 234:H520–524.
20. Grant DA (1999) Ventricular constraint in the fetus and newborn. *Can J Cardiol* 15:95–104.
21. Geiger B, Spatz JP, Bershadsky AD (2009) Environmental sensing through focal adhesions. *Nat Rev Mol Cell Biol* 10:21–33.
22. Wang N, Butler JP, Ingber DE (1993) Mechanotransduction across the cell surface and through the cytoskeleton. *Science* 260:1124–1127.
23. Ingber D (1991) Integrins as mechanochemical transducers. *Curr Opin Cell Biol* 3:841–848.
24. Bellin RM, et al. (2009) Defining the role of syndecan-4 in mechanotransduction using surface-modification approaches. *Proc Natl Acad Sci USA* 106:22102–22107.
25. Chopra A, Tabdanov E, Patel H, Janmey PA, Kresh JY (2011) Cardiac myocyte remodeling mediated by N-cadherin-dependent mechanosensing. *Am J Physiol Heart Circ Physiol* 300:H1252–1266.
26. le Duc Q, et al. (2010) Vinculin potentiates E-cadherin mechanosensing and is recruited to actin-anchored sites within adherens junctions in a myosin II-dependent manner. *J Cell Biol* 189:1107–1115.
27. Liu Z, et al. (2010) Mechanical tugging force regulates the size of cell–cell junctions. *Proc Natl Acad Sci USA* 107:9944–9949.
28. Zhuang J, Yamada KA, Saffitz JE, Kleber AG (2000) Pulsatile stretch remodels cell-to-cell communication in cultured myocytes. *Circ Res* 87:316–322.
29. Birukov KG, et al. (2003) Magnitude-dependent regulation of pulmonary endothelial cell barrier function by cyclic stretch. *Am J Physiol Lung Cell Mol Physiol* 285:L785–797.
30. Krishnan R, et al. (2011) Substrate stiffening promotes endothelial monolayer disruption through enhanced physical forces. *Am J Physiol Cell Physiol* 300:C146–154.
31. Kim JH, Asthagiri AR (2011) Matrix stiffening sensitizes epithelial cells to EGF and enables the loss of contact inhibition of proliferation. *J Cell Sci* 124:1280–1287.
32. Guo WH, Frey MT, Burnham NA, Wang YL (2006) Substrate rigidity regulates the formation and maintenance of tissues. *Biophys J* 90:2213–2220.
33. Berry MF, et al. (2006) Mesenchymal stem cell injection after myocardial infarction improves myocardial compliance. *Am J Physiol Heart Circ Physiol* 290:H2196–2203.
34. Farhadian F, et al. (1995) Fibronectin expression during physiological and pathological cardiac growth. *J Mol Cell Cardiol* 27:981–990.
35. Engler AJ, et al. (2008) Embryonic cardiomyocytes beat best on a matrix with heart-like elasticity: Scar-like rigidity inhibits beating. *J Cell Sci* 121:3794–3802.
36. Pedrotty DM, et al. (2008) Structural coupling of cardiomyocytes and noncardiomyocytes: Quantitative comparisons using a novel micropatterned cell pair assay. *Am J Physiol Heart Circ Physiol* 295:H390–400.
37. Grosberg A, et al. (2011) Self -organization of muscle cell structure and function. *PLoS Comput Biol* 7:e1001088.
38. Butler JP, Tolic-Norrelykke IM, Fabry B, Fredberg JJ (2002) Traction fields, moments, and strain energy that cells exert on their surroundings. *Am J Physiol Cell Physiol* 282:C595–605.
39. McCain ML, et al. (2012) Cell-to-cell coupling in engineered pairs of rat ventricular cardiomyocytes: Relation between Cx43 immunofluorescence and intercellular electrical conductance. *Am J Physiol Heart Circ Physiol* 302:H443–450.
40. Maruthamuthu V, Sabass B, Schwarz US, Gardel ML (2011) Cell-ECM traction force modulates endogenous tension at cell–cell contacts. *Proc Natl Acad Sci USA* 108:4708–4713.
41. Jacot JG, McCulloch AD, Omens JH (2008) Substrate stiffness affects the functional maturation of neonatal rat ventricular myocytes. *Biophys J* 95:3479–3487.
42. Zhu J, Sabharwal T, Kalyanasundaram A, Guo L, Wang G (2009) Topographic mapping and compression elasticity analysis of skinned cardiac muscle fibers in vitro with atomic force microscopy and nanoindentation. *J Biomech* 42:2143–2150.
43. Shiels HA, White E (2008) The Frank–Starling mechanism in vertebrate cardiac myocytes. *J Exp Biol* 211:2005–2013.
44. Prosser BL, Ward CW, Lederer WJ (2011) X-ROS signaling: Rapid mechano-chemo transduction in heart. *Science* 333:1440–1445.
45. Harrison TR, Dixon K, Russell RO, Jr, Bidwai PS, Coleman HN (1964) The relation of age to the duration of contraction, ejection, and relaxation of the normal human heart. *Am Heart J* 67:189–199.
46. Lakatta EG, Gerstenblith G, Angell CS, Shock NW, Weisfeldt ML (1975) Prolonged contraction duration in aged myocardium. *J Clin Invest* 55:61–68.
47. Kushnir A, Shan J, Betzenhauser MJ, Reiken S, Marks AR (2010) Role of CaMKIIdelta phosphorylation of the cardiac ryanodine receptor in the force frequency relationship and heart failure. *Proc Natl Acad Sci USA* 107:10274–10279.
48. Gerdes AM (2002) Cardiac myocyte remodeling in hypertrophy and progression to failure. *J Card Fail* 8:S264–S268.
49. McCain ML, Parker KK (2011) Mechanotransduction: The role of mechanical stress, myocyte shape, and cytoskeletal architecture on cardiac function. *Pflugers Arch* 462:89–104.
50. Dejana E, Tournier-Lasserve E, Weinstein BM (2009) The control of vascular integrity by endothelial cell junctions: Molecular basis and pathological implications. *Dev Cell* 16:209–221.
51. Baumgartner W, et al. (2000) Cadherin interaction probed by atomic force microscopy. *Proc Natl Acad Sci USA* 97:4005–4010.
52. Kokkoli E, Ochsenhirt SE, Tirrell M (2004) Collective and single-molecule interactions of alpha5beta1 integrins. *Langmuir* 20:2397–2404.
53. Zhang Y, Sivasankar S, Nelson WJ, Chu S (2009) Resolving cadherin interactions and binding cooperativity at the single-molecule level. *Proc Natl Acad Sci USA* 106:109–114.
54. Sheehy SP, Huang S, Parker KK (2009) Time-warped comparison of gene expression in adaptive and maladaptive cardiac hypertrophy. *Circ Cardiovasc Genet* 2:116–124.
55. Olson TM, et al. (2002) Metavinculin mutations alter actin interaction in dilated cardiomyopathy. *Circulation* 105:431–437.
56. Delmar M, McKenna WJ (2010) The cardiac desmosome and arrhythmogenic cardiomyopathies: From gene to disease. *Circ Res* 107:700–714.
57. Asimaki A, et al. (2009) A new diagnostic test for arrhythmogenic right ventricular cardiomyopathy. *N Engl J Med* 360:1075–1084.
58. Kostetskii I, et al. (2005) Induced deletion of the N-cadherin gene in the heart leads to dissolution of the intercalated disc structure. *Circ Res* 96:346–354.
59. Aratyn-Schaus Y, Oakes PW, Stricker J, Winter SP, Gardel ML (2010) Preparation of complaint matrices for quantifying cellular contraction. *J Vis Exp* 46:e2173.
60. Radmacher M, Fritz M, Hansma PK (1995) Imaging soft samples with the atomic force microscope: Gelatin in water and propanol. *Biophys J* 69:264–270.
61. Chen CS, Mrksich M, Huang S, Whitesides GM, Ingber DE (1997) Geometric control of cell life and death. *Science* 276:1425–1428.
62. Hynd MR, Frampton JP, Dowell-Mesfin N, Turner JN, Shain W (2007) Directed cell growth on protein-functionalized hydrogel surfaces. *J Neurosci Methods* 162:255–263.

Supporting Information

McCain et al. 10.1073/pnas.1203007109

SI Materials and Methods

Photolithography and Microcontact Printing. Photolithographic masks for microcontact printing (1) were designed in AutoCAD (Autodesk Inc.). One mask consisted of rectangles 12 μm wide and 40–160 μm long. The second mask, which was used for all traction force microscopy (TFM) studies, consisted of rectangles of approximately 1,200 μm² surface area and variable length to width ratios (2 : 25 μm × 50 μm; 4 : 17 μm × 68 μm; 8 : 12 μm × 96 μm; 12 : 10 μm × 120 μm). Our mask design also included an indexing system, allowing us to track the locations of μtissues throughout our experimental protocols. Silicon wafers (Wafer World) spin-coated with SU-8 2002 photoresist (MicroChem Corp) were positioned under the custom photomasks using a mask aligner (ABM Inc.). Wafers were then exposed to UV light, submerged in propylene glycol methyl ether acetate to dissolve masked regions, and used as templates for making polydimethylsiloxane (PDMS, Sylgard 184, Dow Corning) stamps. Fabricated PDMS stamps were coated with 25 μg/mL human fibronectin (FN) (BD Biosciences) for stamping on PDMS coverslips or 200 μg/mL biotinylated FN for stamping on streptavidin-doped polyacrylamide gels and incubated for 1 h. Glass coverslips spin-coated with PDMS were treated in a UV-ozone cleaner (Jelight Company, Inc.) immediately prior to stamping with FN. Polyacrylamide gels doped with streptavidin-acrylamide were dried prior to stamping with biotinylated FN. Stamps coated with FN or biotinylated-FN were dried and inverted onto the coverslip or gel, respectively, to transfer the protein. After stamping, PDMS coverslips were incubated in 1% Pluronic F108 (BASF) to prevent cell adhesion to unstamped regions.

Cell Culture. All procedures were conducted according to the guidelines of the Harvard University Animal Care and Use Committee. Ventricles from 2-d old Sprague–Dawley rat hearts were explanted and minced and a cell suspension was obtained by incubating the tissue with 1 mg/mL trypsin at 4 °C for 12 h, followed by four 1 mg/mL collagenase (Worthington Biochemical Corp.) digestion steps at 37 °C for 2 min each. To decrease non-myocyte cell populations, the cell suspension was preplated twice for 45 min. The cell suspension was then seeded on the patterned coverslips at a concentration of 15,000–50,000 cells/cm². Epinephrine (0.2 μM) was added for the first 24 h in culture. Cultures were maintained in M199 media supplemented with 10% heat-inactivated fetal bovine serum (FBS), 10 mM Hepes, 0.1 mM MEM nonessential amino acids, 20 mM glucose, 2 mM L-glutamine, 1.5 μM vitamin B-12, and 50 U/mL penicillin for the first 2 d in culture, at which point the FBS concentration was lowered to 2% for the remaining days in culture. Epinephrine (0.2 μM) was added again for the final 24 h in culture to maintain spontaneous beating.

Dual Voltage Clamp Recordings of Intercellular Conductance. The EPC 10 USB Double Patch Clamp Amplifier (HEKA Electronic) was used to measure junctional conductance using previously described protocols (2). Briefly, myocyte μtissues cultured on PDMS for 3–5 d were selected for dual voltage clamp experiments using the whole-cell recording mode at room temperature. Blebbistatin (10 μM) was added immediately before beginning experiments to block contraction (3), which can interfere with seal formation between the pipette and cell membrane. After establishing giga-seals on each cell membrane, the membrane potential of both cells was clamped to the same voltage ($V_{\text{cell2}} = V_{\text{cell1}} = 0$ mV) to eliminate transjunctional voltage

($V_J = V_{\text{cell1}} - V_{\text{cell2}}$). Cell 1 was then stimulated with a 10 mV voltage pulse ($V_J = 10$ mV) and current was measured from both cells ($I_{\text{cell1}} = -I_{\text{cell2}}$). The junctional conductance was then determined after correcting for series resistance (4) using previously published values (2).

Cell Fixation, Staining, and Confocal Imaging. Myocytes were fixed by applying 4% paraformaldehyde and 0.5% Triton-X 100 for 5 min at room temperature. Cells were immunostained by incubating with combinations of primary antibodies for the following antigens for 1–2 h at room temperature: Cx43 (MAB3068; Millipore), β-catenin (C2206; Sigma-Aldrich), fibronectin (F2648; Sigma-Aldrich), and paxillin (610051; BD Transduction Laboratories). Alexa Fluor 488, 546, or 633 secondary antibodies (Invitrogen) against the appropriate primary antibody were then added for 1–2 h at room temperature. Cells were also incubated with DAPI and Alexa Fluor 488-, 546-, or 633-conjugated Phalloidin (Invitrogen) to stain for nuclei and actin, respectively. Stained cells were imaged with a Zeiss LSM 5 LIVE confocal microscope.

Image Processing and Quantification of Myocyte Morphology. To quantify the time scale of myocyte spreading, we fixed μtissues cultured on PDMS coverslips with isotropic or micropatterned FN and stained for actin and fibronectin after 2, 4, 8, 12, 24, and 96 h. We imaged FN islands with conserved width (12 μm) and lengths of 40, 60, and 80 μm occupied by exactly two myocytes at each time point. We then manually outlined the cell borders to quantify the area of the myocyte μtissue and divided the total μtissue area by the area of the FN island to determine the percentage of FN island coverage.

To quantify junction shape, the widths and lengths of μtissues stained for actin, β-catenin, and nuclei were measured in ImageJ (NIH) and the ratio of length to width was defined as μtissue length to width ratio (μLW). We defined the longitudinal axis of the μtissue as the x axis and the transverse axis as the y axis. Points along the cell–cell junction, as indicated by β-catenin immunostains, were manually selected and fit to the equation for the logistic function, which we defined as f_J, using the curve fitting toolbox in MATLAB (MathWorks) to determine a and b:

$$f_J = \frac{a}{1 + e^{-bx}}. \qquad \textbf{[S1]}$$

To quantify myofibril structure, the maximum intensity projections of μtissues stained for actin were generated from confocal z-stacks. The maximum projection image was input into custom MATLAB (MathWorks) code for detecting actin alignment based on a fingerprint detection algorithm, as previously described (5). The orientational order parameter (OOP) was calculated for each distribution of actin orientation angles. The OOP is a commonly used metric that characterizes the degree of orientational order, with the parameter 0 for isotropic systems and 1 for perfectly aligned systems (6–8).

TFM of Micropatterned Myocytes. After 4 d in culture, micropatterned myocytes on polyacrylamide gels were moved to an incubation chamber on a Zeiss LSM 5 Live confocal microscope maintained at 37 °C and immersed in Tyrode's solution (1.8 mM CaCl₂, 5 mM glucose, 5 mM Hepes, 1 mM MgCl₂, 5.4 mM KCl, 135 mM NaCl, 0.33 mM NaH₂PO₄, pH 7.4). Spontaneously contracting myocyte μtissues were imaged with a 40X

Plan-Apochromat oil objective at 40 Hz with both brightfield and 488 laser excitation to obtain movies of myocytes contracting and displacing fluorescent beads in the gel substrate over multiple contractile cycles. Following the experiment, coverslips were fixed, immunostained for β-catenin, and imaged with a confocal microscope using the same protocol described above to identify the cell–cell junction.

TFM Data Analysis. The methods used to acquire displacement and traction stress vectors from images of bead displacement have been previously described (7, 9). Briefly, displacement of the gel was determined by comparing bead images throughout the contraction cycle to the bead image at diastole. The traction stress field was then calculated from the displacement map using Fourier transform traction cytometry methods. Traction stress vectors were discretized to a 5×5 μm^2 grid.

To plot maximum traction stress versus maximum displacement in the longitudinal direction, the magnitude of the maximum traction stress vector ($\max.|\sigma_{x,\mu\text{tissue}}|$) was plotted against the maximum displacement vector ($\max.|\Delta x_{\mu\text{tissue}}|$) in the x-direction for single contraction cycles for multiple μtissues on soft, moderate, and stiff gels. To calculate the duration of contraction cycles, the length of time a given μtissue maintained $\max.$ $|\sigma_{x,\mu\text{tissue}}|$ greater than 50% peak systolic $\max.|\sigma_{x,\mu\text{tissue}}|$ was determined.

To calculate the average longitudinal tension through a cross-section of a given μtissue, we applied the following equation from continuum mechanics for calculating the average stress in a body (10):

$$\sigma_{ij} = \frac{1}{V} \int_S T_i r_j dS, \qquad [\text{S2}]$$

where V and S are the volume and surface area of the body, respectively; T_i is the traction force vector in the i-direction; and r_j is the position of the vector in the j-direction on the surface of the body. Note that this equation is not dependent on the location of the origin or the orientation of the coordinate system. Using the coordinate system shown in Fig. 2E, the average longitudinal stress in a μtissue is represented by σ_{xx}. We multiplied σ_{xx} by the cross-sectional area of the μtissue, $V_{\mu\text{tissue}}/L_{\mu\text{tissue}}$, where $V_{\mu\text{tissue}}$ is the volume and $L_{\mu\text{tissue}}$ is the length of the μtissue, to calculate the average longitudinal tension through a cross-section of the μtissue, $N_{xx,\mu\text{tissue}}$:

$$N_{xx,\mu\text{tissue}} = \frac{V_{\mu\text{tissue}}\sigma_{xx}}{L_{\mu\text{tissue}}} = \frac{1}{L_{\mu\text{tissue}}} \int_{\mu\text{tissue}} T_x r_x dS. \qquad [\text{S3}]$$

The discretized form of $N_{xx,\mu\text{tissue}}$ is

$$N_{xx,\mu\text{tissue}} = \frac{1}{L_{\mu\text{tissue}}} \sum_{\mu\text{tissue}} T_{x,n} r_{x,n}. \qquad [\text{S4}]$$

To apply this equation to our TFM data set, we multiplied the traction stress vectors for a given field of view by the surface area of the grid square (25 μm^2) to determine the traction force vectors ($\vec{T}_n$) for each grid square, n, with the x-position, $r_{x,n}$.

To calculate the average longitudinal tension in a single cell within a μtissue ($N_{xx,\text{cell}}$), we applied Eq. **S3** with an added term for force at the cell–cell junction:

$$N_{xx,\text{cell}} = \frac{1}{L_{\text{cell}}} \int_{S_{\text{cell}}} T_x r_x dS + \frac{1}{L_{\text{cell}}} \int_{S_{\text{junction}}} T_x r_x dS. \qquad [\text{S5}]$$

We estimated L_{cell} as the length of the cell at its central axis. Similarly, we estimated the x-position of the junction ($r_{x,\text{junction}}$) as the x-position at its central axis. Thus, Eq. **S5** becomes

$$N_{xx,\text{cell}} = \frac{1}{L_{\text{cell}}} \int_{S_{\text{cell}}} T_x r_x dS + \frac{r_{x,\text{junction}}}{L_{\text{cell}}} \int_{S_{\text{junction}}} T_x dS. \qquad [\text{S6}]$$

For each μtissue, we shifted our coordinate system so that $r_{x,\text{junction}} = 0$, which eliminates the second term of Eq. **S6**. Thus, the discretized equation we applied to calculate $N_{xx,\text{cell}}$ is

$$N_{xx,\text{cell}} = \frac{1}{L_{\text{cell}}} \sum_{\text{cell}} T_{x,n} r_{x,n}. \qquad [\text{S7}]$$

The techniques used to calculate cell–cell junction force are based on a previously published TFM study (11). The cell–cell interface in μtissues was identified using the β-catenin immunosignal collected after each TFM experiment. We manually traced the cell–cell junction and used the junction contour to separate the $\vec{T}_n$ maps into two halves, with the left and right halves representing $\vec{T}_n$ contributed by the left (cell 1) and right (cell 2) myocytes, respectively. The unbalanced traction force vector for cell 1 ($\vec{F}_{\text{unbalanced }T,\text{Cell1}}$) was then calculated by vectorially summing $\vec{T}_n$ in the field of view corresponding to cell 1:

$$\vec{F}_{\text{unbalanced }T,\text{Cell1}} = \sum_{\text{Cell1}} \vec{T}_n. \qquad [\text{S8}]$$

$\vec{F}_{\text{unbalanced }T,\text{Cell1}}$ was nonzero because each cell generates force against both the ECM and the cell–cell junction, but this force vector only accounts for forces exerted against the ECM. Because each cell is in mechanical equilibrium, $\vec{F}_{\text{unbalanced }T,\text{Cell1}}$ must be balanced by the amount of force exerted against the cell–cell junction ($\vec{F}_{J,\text{Cell1}}$):

$$\vec{F}_{\text{unbalanced }T,\text{Cell1}} + \vec{F}_{J,\text{Cell1}} = 0. \qquad [\text{S9}]$$

Therefore, $\vec{F}_{J,\text{Cell1}}$ can be calculated from the $\vec{T}_n$ vector field:

$$\vec{F}_{J,\text{Cell1}} = -\vec{F}_{\text{unbalanced }T,\text{Cell1}} = -\sum_{\text{Cell1}} \vec{T}_n. \qquad [\text{S10}]$$

The magnitude of the x-component of $\vec{F}_{J,\text{Cell1}}$ ($F_{x,J,\text{Cell1}} = |\sum_{\text{Cell}} T_{x,n}|$) represents the longitudinal force applied to the cell–cell junction. The magnitude of $\vec{F}_{J,\text{Cell1}}$ indicates the total force applied to the cell–cell junction by cell 1 ($F_{J,\text{Cell1}}$):

$$F_{J,\text{Cell1}} = |\sum_{\text{Cell1}} \vec{T}_n|. \qquad [\text{S11}]$$

The same analysis procedure was followed to calculate cell–cell junction forces generated by cell 2.

To calculate work generated by a given μtissue, we adapted previously published methods (9) and applied this equation:

$$\text{Work} = \frac{1}{2} \sum_{\mu\text{tissue}} (u_{x,n} T_{x,n} + u_{y,n} T_{y,n}), \qquad [\text{S12}]$$

where u_i represents displacement in the i-direction.

1. Chen CS, Mrksich M, Huang S, Whitesides GM, Ingber DE (1997) Geometric control of cell life and death. *Science* 276:1425–1428.

2. McCain ML, et al. (2012) Cell-to-cell coupling in engineered pairs of rat ventricular cardiomyocytes: Relation between Cx43 immunofluorescence and intercellular electrical conductance. *Am J Physiol Heart Circ Physiol* 302:H443–H450.

3. Fedorov VV, et al. (2007) Application of blebbistatin as an excitation-contraction uncoupler for electrophysiologic study of rat and rabbit hearts. *Heart Rhythm* 4:619–626.
4. Van Rijen HV, Wilders R, Van Ginneken AC, Jongsma HJ (1998) Quantitative analysis of dual whole-cell voltage-clamp determination of gap junctional conductance. *Pflugers Arch* 436:141–151.
5. Bray MA, Sheehy SP, Parker KK (2008) Sarcomere alignment is regulated by myocyte shape. *Cell Motil Cytoskeleton* 65:641–651.
6. Grosberg A, Alford PW, McCain ML, Parker KK (2011) Ensembles of engineered cardiac tissues for physiological and pharmacological study: Heart on a chip. *Lab Chip* 11:4165–4173.
7. Grosberg A, et al. (2011) Self-organization of muscle cell structure and function. *PLoS Comput Biol* 7:e1001088.
8. Volfson D, Cookson S, Hasty J, Tsimring LS (2008) Biomechanical ordering of dense cell populations. *Proc Natl Acad Sci USA* 105:15346–15351.
9. Butler JP, Tolic-Norrelykke IM, Fabry B, Fredberg JJ (2002) Traction fields, moments, and strain energy that cells exert on their surroundings. *Am J Physiol Cell Physiol* 282:C595–605.
10. Landau LD, Lifshitz EM (1986) *Theory of Elasticity* (Elsevier, New York), 3rd Ed, pp 3–7.
11. Maruthamuthu V, Sabass B, Schwarz US, Gardel ML (2011) Cell-ECM traction force modulates endogenous tension at cell–cell contacts. *Proc Natl Acad Sci USA* 108:4708–4713.
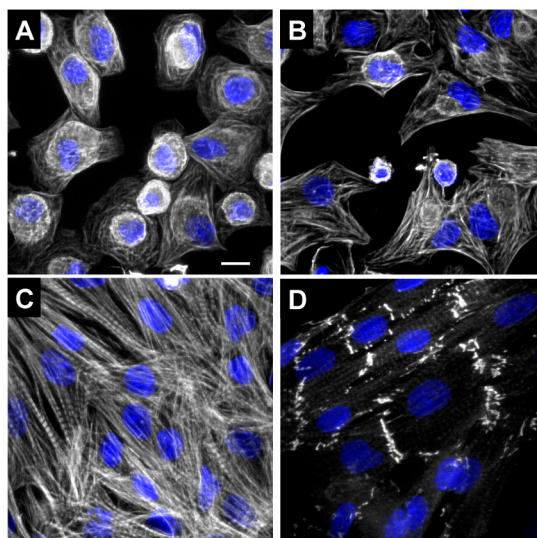
Fig. S1. Tissue formation on unpatterned substrates. Myocytes cultured on uniform FN for 4 h (*A*) and 8 h (*B*) were spreading, pleomorphic, and nonstriated. (*C*) After 12 h in culture, myocytes formed into a confluent, isotropic tissue with striated myofibrils. (*A*–*C*) White: actin, blue: nuclei. (*D*) Myocytes grown on uniform FN for 4 d did not couple with sigmoidal interfaces. Instead, cell–cell junctions were primarily perpendicular to myofibrils (white: β-catenin, blue: nuclei). (Scale bar: 10 μm.)
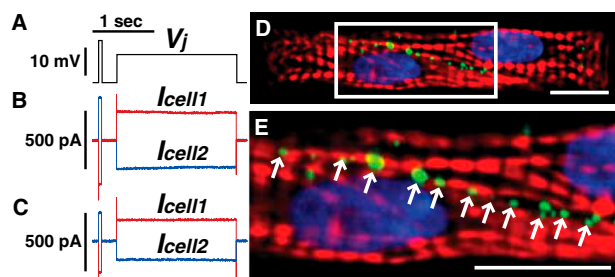

Fig. S2. Electrical coupling of μtissues. (*A*) Dual voltage clamp recordings were performed by attaching patch clamp electrodes to the membrane of each myocyte and applying voltage pulses to only one cell in the μtissue using the voltage protocol shown ($V_j = V_{cell1} - V_{cell2}$). Electrical current flowing through the junction was measured with each electrode ($I_{cell1} = -I_{cell2}$). The measured values, corrected with an electrode access resistance of 9.1 MOhms, corresponded to an intercellular electrical conductance of 43.4 nS for a μtissue with μLW 3.5 (*B*) and 24.9 nS for a μtissue with μLW 7.1 (*C*). (*D* and *E*) Gap junction formation was confirmed by immunostaining μtissues for Cx43 (green: Cx43, red: actin, blue: nuclei, *E* corresponds to the boxed portion of *D*). Gap junction channels were routinely detected along the cell–cell interface (white arrows in *E*). (Scale bars: 10 μm.)
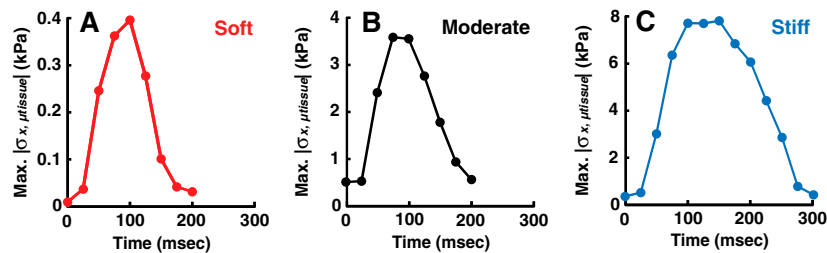
Fig. S3. Contraction cycle dynamics as a function of substrate stiffness. Plots of max. $|\sigma_{x,\mu tissue}|$ over a single contraction cycle for representative μLW 12 μtissues on soft (*A*), moderate (*B*), and stiff (*C*) substrates.
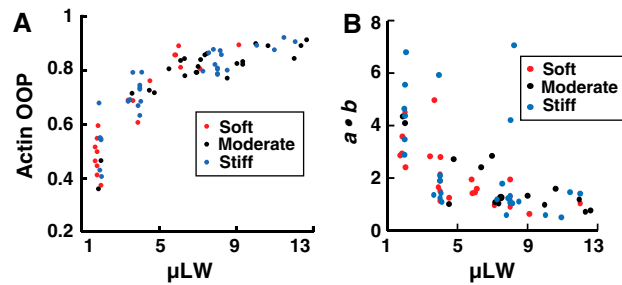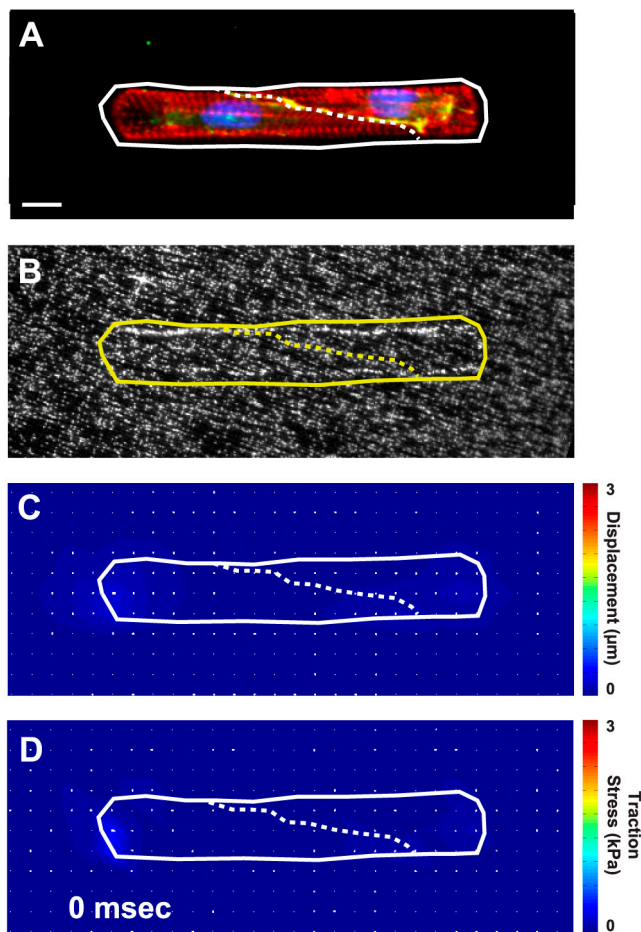

Fig. S4. Actin orientation and junction slope is independent of substrate stiffness. The actin OOP similarly increased (*A*) and sigmoid junction parameter $a \cdot b$ similarly decreased (*B*) with μLW for μtissues on all substrates.
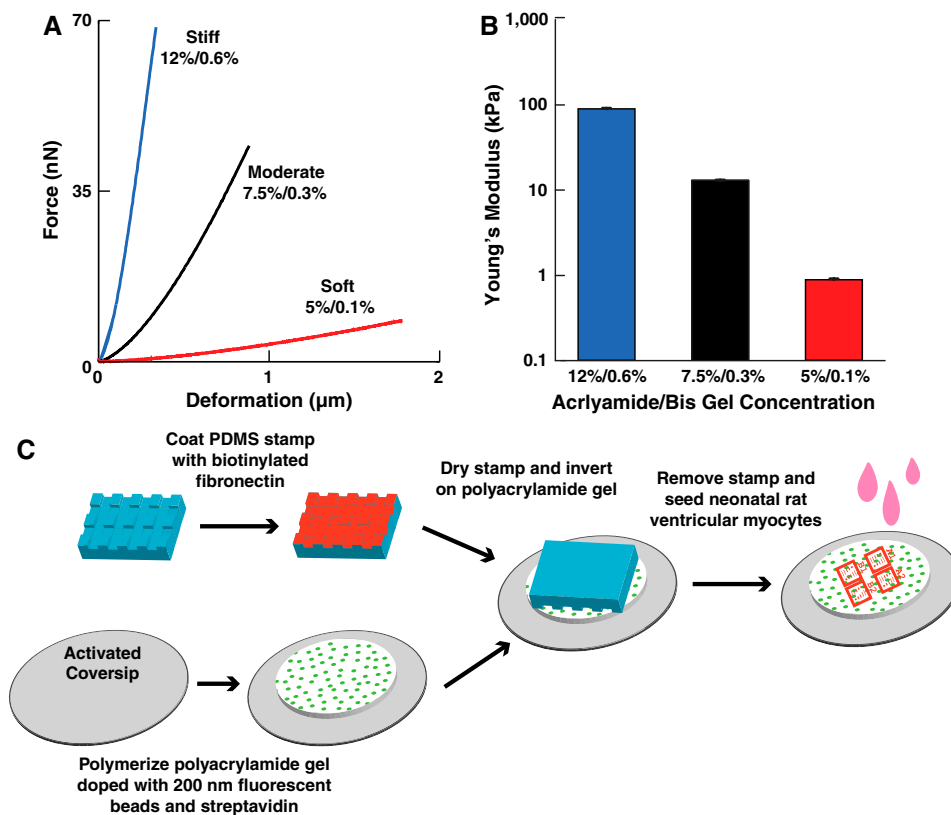
Fig. S5. Stiffness validation and microcontact printing of polyacrylamide gels. (*A*) Atomic force microscopy was used to measure force-deformation curves for polyacrylamide gels with the indicated acrylamide/bis gel concentrations. (*B*) The elastic modulus for each acrylamide/bis gel concentration was calculated from the force-deformation curves. (*C*) Schematic of microcontact printing protocol for polyacrylamide gels.

Movie S1. Contracting Day 1 µtissue. (*A*) Immunofluorescent image of µtissue cultured for one day (red: actin, green: β-catenin, blue: nuclei). (*B*) As the µtissue spontaneously contracted, beads in the substrate displaced and were tracked to calculate displacement (*C*) and traction stress (*D*) vector maps. In all panels, solid lines indicate µtissue outline and dashed lines indicate cell–cell junction. Note that the myocytes are not completely synchronous and traction is detected near the cell–cell interface at peak systole. (Scale bar: 10 µm.)

Movie S1 (AVI)

Movie S2. Contracting Day 4 μtissue. (*A*) Immunofluorescent image of μtissue cultured for 4 d (red: actin, green: β-catenin, blue: nuclei). (*B*) As the μtissue spontaneously contracted, beads in the substrate displaced and were tracked to calculate displacement (*C*) and traction stress (*D*) vector maps. In all panels, solid lines indicate μtissue outline and dashed lines indicate cell–cell junction. Note that the myocytes are synchronous and traction is isolated to the long-itudinal ends of the μtissue at peak systole. (Scale bar: 10 μm.)

Movie S2 (AVI)